Journal of Nuclear Medicine, published on February 9, 2018 as doi:10.2967/jnumed.117.203000

Respiratory Motion Compensation for PET/CT with Motion Information Derived from Matched Attenuation Corrected Gated PET Data

Yihuan Lu[1], Kathryn Fontaine[1], Tim Mulnix[1], John A. Onofrey[1], Silin Ren[2], Vladimir Panin[3], Judson Jones[3], Michael E. Casey[3], Robert Barnett[4], Peter Kench[4], Roger Fulton[4], Richard E. Carson[1,2], and Chi Liu[1,2]

[1]Department of Radiology and Biomedical Imaging, Yale University, New Haven, CT, USA

[2]Department of Biomedical Engineering, Yale University, New Haven, CT, USA

[3]Siemens Medical Solutions, Knoxville, TN, USA

[4]Discipline of Medical Radiation Sciences, Faculty of Health Sciences, the University of Sydney, Australia

Funding sources and disclosures:

This work is funded by research contracts from Siemens Medical Solutions and NIH grant S10RR29245.

First author: Yihuan Lu, Ph.D., Department of Radiology and Biomedical Imaging, Yale University, PO Box 208048, New Haven, CT, United States, 06520-8048. E-mail: yihuan.lu@yale.edu. Phone: 2037371214.

Correspondence contact: Yihuan Lu, Ph.D. and Chi Liu, Ph.D., Department of Radiology and Biomedical Imaging, Yale University, PO Box 208048, New Haven, CT, United States, 06520-8048. E-mail: yihuan.lu@yale.edu and chi.liu@yale.edu, Phone: 2037371214 and 2037854269

ABSTRACT

Respiratory motion degrades the detection and quantification capabilities of PET/CT imaging. Moreover, mismatch between a fast helical CT and a time-averaged PET image due to respiratory motion results in additional attenuation correction (AC) artifacts and inaccurate localization. Current motion compensation (MC) approaches typically have three limitations: 1) the mismatch among respiratory-gated PET images and the CTAC map can introduce artifacts in the gated PET reconstructions that can subsequently affect the accuracy of the motion estimation; 2) sinogram-based correction approaches do not correct for intra-gate motion due to intra-cycle and inter-cycle breathing variations; 3) the mismatch between the PET MC-reference gate and CT can cause additional CT-mismatch artifact. In this study, we established a motion correction framework to address these limitations.

Methods: In the proposed framework, the combined emission/transmission reconstruction algorithm was used for phase-matched gated-PET reconstructions to facilitate the motion model building. Event-by-event non-rigid respiratory MC method with correlations between internal organ motion and external respiratory signals was used to correct both intra-cycle and inter-cycle breathing variations. The PET reference gate is automatically determined by a newly proposed CT-matching algorithm. We applied the new framework to 13 human datasets with 3 different radiotracers and in total 323 lesions, and compared its performance with CTAC-based and Non-AC-based (NAC) approaches. Validation using 4D CT was performed for one lung cancer dataset.

Results: For the ten ^{18}F-FDG studies, the proposed method outperformed ($p<0.006$) both CTAC- and NAC-based methods in terms of ROI-based SUV_{mean}, SUV_{max} and SUV-ratio improvements over no motion correction (NMC) (SUV_{mean}: 19.9% vs. 14.0% vs. 13.2%; SUV_{max}: 15.5% vs. 10.8% vs. 10.6%; SUV-ratio: 24.1% vs. 17.6% vs. 16.2%, for the proposed, CTAC- and NAC-based methods, respectively). The proposed method increased SUV-ratio values over NMC for 94.4% lesions compared to 84.8% and 86.4% using CTAC- and NAC-based methods, respectively. For the two ^{18}F-FPDTBZ studies, the proposed method reduced the CT-mismatch artifacts in the lower lung where the CTAC-based approach failed, and maintained the quantification accuracy of bone marrow where the NAC-based approach failed. For the ^{18}F-FMISO study, the proposed method outperformed both CTAC- and NAC-based methods in terms of motion estimation accuracy at two lung lesion locations.

Conclusion: The proposed PET/CT respiratory event-by-event motion-correction framework with motion information derived from matched attenuation corrected PET data provides superior image quality than CTAC- and NAC-based methods for multiple tracers.

Key words: PET, respiratory motion correction, event-by-event, non-rigid, matched attenuation correction

INTRODUCTION

In PET imaging of the thorax and abdomen, respiratory motion degrades the detection and accurate quantification of small nodules and organs (*1*). In addition, the mismatch between a fast helical CT and a time-averaged PET image due to respiratory motion may result in attenuation correction (AC) artifacts (*2*) and inaccurate localization (*3,4*) for PET/CT imaging.

Respiratory gating is the most common approach for addressing motion effects (*5*). However, gated PET suffers from a low signal-to-noise ratio (SNR) due to noise increase by using only a fraction of counts in each gate. Post-reconstruction registration (PRR) (*6*) is one alternative, which non-rigidly registers all the gated PET to a reference gate to improve SNR by using all detected events. Another category of approaches, motion-compensated image reconstruction (MCIR), reconstructs all the gated-PET data into one reference gate by incorporating the non-rigid motion information into the reconstruction (*7*). Both PRR and MCIR typically extract patient-specific motion from gated PET using a deformable registration model. Comparing to images without motion correction, these methods yield higher image contrast and more accurate quantification without amplifying image noise. However, both PRR and MCIR share three major limitations.

First, each gated PET suffers from a CT-mismatch artifact since the fast helical CT scan, at best, matches one respiratory phase of the gated PET. Such artifacts can substantially affect motion estimation accuracy for subsequent motion correction. One example of this mismatch artifact is shown with end-inspiration gated PET (Figure 1A left) reconstructed and superposed with the CT acquired during expiration. The CT-mismatch artifacts appeared at lower lung regions (arrows). In contrast, the end-expiration gated PET (Figure 1A right) well matches CT. One solution is to use non attenuation-corrected (NAC) gated PET to derive registration results (*8*). However, one potential problem with NAC-gated PET is that motion estimation errors may occur due to the inaccurate tracer distributions without attenuation correction, as further demonstrated in this paper.

A second limitation of existing PRR and MCIR approaches is that they do not correct for intra-gate motion, i.e., motion within each gated PET image due to intra-cycle and inter-cycle breathing variations. This is particularly important for irregular breathers with long-term motion variability (*4*). As shown in Figure 1B, more blurring and contrast loss are seen in the end-inspiration than the end-expiration gate, which contains less intra-gate motion.

A third limitation is that if a breath-hold CT is acquired, its phase is typically assumed to be known according to a certain acquisition protocol, such as breath coaching. However, patients often fail to follow the breathing instructions due to anxiousness, confusion, or simply inability to hold their breath due to illness. The inconsistency between the actual CT phase and the presumed CT phase, which is typically considered as the reference gate for PET motion correction, can cause additional CT-mismatch artifacts in motion-corrected reconstructions. Alternatively, if a free-breathing CT is acquired, it will result in mismatch with all the PET gates.

In this work, we propose a framework to address these limitations. First, to obtain gated PET with phase-matched AC to overcome the CT-mismatch problem, we investigated the use of the time-of-flight (TOF) maximum likelihood activity and attenuation correction factors estimation (MLACF) (*9*) algorithm and compared it with CTAC- or NAC-based approaches. Similar to the maximum likelihood attenuation and activity estimation (MLAA) algorithm (*10*), the MLACF algorithm generates attenuation information from PET data, which yields gated PET images with intrinsically matched attenuation correction. Although the MLACF images may not be quantitative (*9*), they can provide useful images to estimate non-rigid motion between gates. Second, to address the intra-gate motion, we incorporated non-rigid motion information derived from MLACF-reconstructed gated PET into the framework of non-rigid *int*ernal-*ex*ternal (NR-INTEX) motion correlation technique (*11*) integrated with *mo*tion-compensation ordered-subsets expectation maximization *l*ist-mode *a*lgorithm for resolution-recovery *r*econstruction (MOLAR) (*12*), for both inter- and intra-gate respiratory motion correction in an event-by-event fashion (*11*). Third, the PET reference gate, where all the events corrected to, is automatically determined by choosing the gate whose MLAA-derived attenuation map best matches the helical CT image.

We name the new framework AIM (*A*PN-*I*NTEX-*M*OLAR), where APN stands for *a*utomated *p*hase-matched *n*onrigid. Our proposed approach was compared to NR-INTEX motion corrections with the motion model derived from CTAC- and NAC-based gated PET (referred as CTAC- and NAC-based approaches) using human data with 3 different tracers.

MATERIALS AND METHODS

Human Subjects and Data Acquisitions

Thirteen human PET/CT datasets with 3 different radiotracers, including ten ^{18}F-FDG, two ^{18}F-fluoropropyl-(+)-dihydrotetrabenazine (FPDTBZ), a radiotracer that binds to the vesicular monoamine transporter-2 in Beta-cells in the pancreas (*13*), and one ^{18}F-fluoromisonidazole (FMISO) (*14*). All studies were approved by the Institutional Review Board and Radiation Safety Committee at Yale University (^{18}F-FPDTBZ and ^{18}F-FMISO) and the University of Sydney (^{18}F-FDG).

For the ten ^{18}F-FDG datasets, eight cancer patients underwent a single-bed scan of 3-5 min. Two patients underwent PET scans with 2 bed positions. For the purpose of evaluating motion correction, we considered each bed position data as an individual study. The mean injection activity was 209±11 MBq. In each of the two abdominal studies performed with ^{18}F-FPDTBZ, data from the first 10 min of the scan was used. The injection dose was 257 MBq and 286 MBq, respectively. For a non-small cell lung cancer patient underwent chest imaging (1 bed position) with 180 MBq injection of ^{18}F-FMISO, and the first 30 min of data were used.

All PET data were obtained in list mode using the 4-ring Siemens Biograph mCT scanners located at the Yale PET Center and Westmead Hospital. External respiratory motion was tracked using the Anzai belt system. The Anzai respiratory trace was recorded at 50 Hz for all subjects except for the two ^{18}F-FPDTBZ subjects (40 Hz). End-expiration breath-hold CT was acquired for FPDTBZ and FMISO subjects while free-breathing CT was acquired for FDG subjects. For the FMISO patient, an additional 4D CT dataset was acquired under normal breathing.

Overview of AIM (APN-INTEX-MOLAR)

A flowchart of the AIM framework is shown in Figure 2 and details are given below. We first determine which of the 8 respiratory phases best matches the CT, which will be used as the reference phase for PET motion correction. Then, a non-rigid motion model is built to describe a continuous relationship between the Anzai displacement and the movement of each voxel (*11*). Finally, the event-by-event motion-corrected reconstruction generates the final image with all the counts corrected to the reference phase (*11*) .

Determination of Reference Phase

The reference phase was chosen to be the one that best matches the helical CT acquired under either breath-hold or free-breathing conditions. In this way, the mismatched AC artifacts can be minimized in the final motion compensated reconstruction. List-mode PET data were histogramed into 8 respiratory gated sinograms based on the Anzai trace. MLAA (*10*) (3 iterations × 21 subsets) was used to reconstruct the attenuation maps (MLAA-μ) for

each gate with the CT-μ as the initial guess. A 3D-Gaussian filter with a full-width-half-maximum (FWHM) of 15 mm was applied to the MLAA-μ images. Pearson's linear correlation coefficients for the entire image between the CT-μ and all MLAA-μ images were calculated. The gate yielding the highest correlation coefficient was chosen as the reference phase.

Motion Model Building and Correction

First, MLACF (*9*) (50 effective iterations) was used to reconstruct each gated PET image. For comparison studies, we also generated gated PET using OSEM (3 iterations × 21 subsets) without attenuation correction (NAC-based) and with CT-μ (CTAC-based), which used a single attenuation map derived from the 3D CT data to reconstruct PET images of all gates. All gated-reconstructions were post smoothed with a 3D Gaussian filter with a 8-mm FWHM.

To obtain inter-gate voxel-by-voxel respiratory motion estimation, non-rigid registrations were performed between the reference gate and the remaining gates, using the BioImage Suite software (*15*). Normalized mutual information was used as the similarity metric and a free-form-deformation (FFD) was used to parameterize the deformation model (*16*). The parameter of control point spacing was chosen to be 30 mm for ^{18}F-FDG and 15 mm for ^{18}F-FPDTBZ and ^{18}F-FMISO. Smaller spacing was preferred for high-count images (^{18}F-FPDTBZ and ^{18}F-FMISO) since it has the potential for more accurate registration by allowing for greater amounts of non-rigid deformations. Larger spacing, on the other hand, is more robust to image noise that is common in low-count images (^{18}F-FDG). The resulting motion vectors were then used as the inter-gate motion estimates in X (left-right), Y (anterior-posterior) and Z (superior-inferior) directions for each voxel.

Based on the inter-gate motion estimates, a linear *motion model* was built between each voxel's movement in X, Y and Z directions and the *mean* Anzai displacement corresponding to each gate. Thus both Anzai and inter-gate motion estimates are for "average locations" within each gate. Although the correlation for every voxel was built against the *same* mean displacements of Anzai trace, the inter-gate motion estimate is different for each voxel, forming the non-rigid nature of the framework. This non-rigid model can be used to describe a *continuous* relationship between the Anzai trace displacement and the movement of each voxel, which were subsequently incorporated into non-rigid INTEX-MOLAR to perform event-by-event motion compensated list-mode OSEM reconstruction (3 iterations x 21 subsets). Further details on the non-rigid INTEX-MOLAR method were described

in (*11*). Decay, scatter and random corrections were performed. A 3D Gaussian filter with a 3-mm FWHM was applied for post-reconstruction smoothing.

Image Analysis and 4D CT Validation

To quantitatively evaluate AIM, changes in SUV_{mean}, SUV_{max}, SUR (the SUV Ratio between lesion SUV_{mean} and blood pool SUV_{mean}), coefficient of variation of a uniform organ (e.g. liver), and signal-to-noise ratio (SNR), as compared to no motion correction (NMC) data were reported. The mean and standard deviation of improvement across different lesion and organ ROIs within a subject is reported. Ellipsoid ROIs were used for all studies except pancreas and kidney for ^{18}F-FPDTBZ and the large tumor for ^{18}F-FMISO, where manually-drawn ROIs were used. For each target organ, the size of the ROI was kept constant across all methods, while the ROI location was re-centered for each method. All the methods used the *same MLAA-determined CT phase* as the reference phase. For the ^{18}F-FDG studies, the 2-tailed Wilcoxon signed-rank test was used to test for significant differences between AIM, CTAC-based, and NAC-based methods in terms of SUV_{mean}, SUV_{max}, and SUR.

For the 4D-CT in ^{18}F-FMISO study, eight respiratory-gated CT attenuation maps (μ_{4DCT}) were generated. Non-rigid registrations were performed between the reference gate and the remaining gates. Registrations generated inter-gate motion vectors based on 4D-CT were considered as the gold standard motion vectors for comparison to the PET motion vector estimation. To calculate residual error, the 3D attenuation CT-μ was warped using the gated PET-derived motion model to each respiratory gate to generate *synthetic* 4D-CT (μ_{Syn}). Note that the 3D attenuation CT was taken before the PET scan and the 4D-CT was taken after the PET scan. The difference between μ_{4DCT} and μ_{Syn} within an ROI for the g^{th} *gate* was calculated using:

$$\mu Err\%(g) = \underset{ROI}{mean} \frac{\mu_{Syn}(g) - \mu_{4DCT}(g)}{\mu_{4DCT}(g)} \times 100\%$$

$\mu Err\%(g)$ was computed within ROIs at the liver dome (52.6 cm^3), large tumor (85.7 cm^3), and small tumor (10.7 cm^3).

RESULTS

For 2 out of 3 breath-hold CT studies, the CT scan was not acquired during the targeted phase. The reference phase determination method identified the phase that best matches the CT and was confirmed visually by carefully examining the supposition of the CT and gated PET in image domain. Detailed results on reference phase determination for all subjects can be found in Supplemental Table 1.

Figure 3 shows sample EE images from ^{18}F-FPDTBZ study #1 using different AC methods and the corresponding motion vectors from EI to EE phases. Since the CT image was acquired at EE phase, CTAC-based image shows the "banana" artifact at the lung-liver and lung-spleen interfaces (black arrows), due to the mismatch between CT and PET. NAC-based images did not suffer from this artifact. However, due to greater attenuation in the center of the body, the spine region in NAC images was substantially underestimated (white arrow). In contrast, the proposed MLACF-based reconstruction did not suffer from AC-mismatch artifact nor underestimation in the spine region. Motion vectors based on CTAC-based images were underestimated in the "banana" artifact regions, since the artifact was only present in the EI images, which lead to inaccurate motion estimation. For the NAC-based result, unrealistic motions in the vertical direction were estimated in the spine region, which should not move during breathing. Such spine motion vectors were likely introduced by its neighboring high-uptake organs, such as kidneys and liver. In contrast, motion vectors generated by the MLACF-based method appear to be reasonable in all regions. Specifically, a vertical gradient in vector length (larger closer to the diaphragm) was observed, which is consistent with respiratory movement driven by diaphragm.

Figure 4(A) shows the difference maps between μ_{4DCT} and μ_{Syn} generated by the three different methods around the large-tumor region for the ^{18}F-FMISO study and Figure 4(B) shows for the liver-dome region. CTAC-based μ_{Syn} yielded the largest visual discrepancy comparing to μ_{4DCT} while AIM yields the smallest. Quantitative measurements (Table 1) confirmed that among the three methods, AIM provided the smallest mean and standard deviation of $\mu Err\%(g)$ across all gates, indicating that the AIM-generated motion model is the most accurate among the three methods. The remaining error in $\mu Err\%(g)$ could be due to the fact that the 4D-CT and PET-CT data were acquired at different times with potential breathing pattern difference. Additional validation results for the small tumor can be found in the Supplemental Figure 1. Also, a video showing a comparison between μ_{4DCT} and μ_{Syn} generated by AIM can be found in Supplemental Video 1.

Respiratory Motion Correction

Sample results from ^{18}F-FDG studies are shown in Figure 5. Figure 5(A) shows that the CTAC-based method partially restored the liver-lesion shape and contrast (SUV_{mean}= 6.4 comparing to 5.5 with NMC) while both NAC-based (SUV_{mean}=8.7) and AIM (SUV_{mean}=8.8) showed a substantial improvement. The spine tumor (Figure 5(B)) has the highest contrast with NMC (SUV_{mean} =7.7), which is expected since the spine position was unaffected by respiration. AIM (SUV_{mean} =7.5) and CTAC-based (SUV_{mean} =7.5) methods performed equally well in keeping the spine static, while the NAC-based (SUV_{mean} =4.6) method introduced blurring. Figure 5(C-D) showed that AIM achieved the highest tumor contrast and the smallest apparent tumor volume among the three methods.

Quantitatively, for ^{18}F-FDG studies (Table 2), CTAC- and NAC- based methods provided similar increases in terms of averaged SUV_{mean} (14.0% vs. 13.2%), SUV_{max} (10.8% vs. 10.6%) and SUR (17.6% vs. 16.2%). No statistical significance ($p>0.05$) was found between CTAC- and NAC- based methods for any metrics. However, the AIM method (SUV_{mean} 19.9%, SUV_{max} 15.5%, SUR 24.1%) significantly outperformed CTAC- and NAC-based methods for all metrics ($p<0.006$). The NAC-based method outperformed CTAC-based method for lesions close to the lung-liver boundary, likely due to AC artifact, while CTAC-based method outperformed NAC-based method for lesions located in the body center. In contrast, AIM consistently outperformed both CTAC- and NAC-based methods for nearly all lesions independent of their locations. Overall, AIM increased SUR values over NMC for 94.4% lesions (323 in total) as compared to 84.8% and 86.4% for CTAC- and NAC-based methods, respectively (Supplemental Figure 2). For a subset of 65 lesions located close to the *liver boundary and lung boundary*, we observed a larger improvement for AIM comparing to CTAC- and NAC- methods in SUV_{mean} (26.1% vs. 11.2% and 15.4%), SUV_{max} (26.9% vs. 8.1% and 16.0%) and SUR (27.5% vs. 10.7% and 14.6%).

As shown in Figure 6(A), due to mismatched AC, the “banana” artifact induced motion-estimation errors that propagated to the motion-compensated reconstruction (black arrow) for the CTAC-based method, which had only marginal artifact reduction compared to NMC. In contrast, both NAC-based method and AIM largely removed this artifact. Figure 6(B) shows that the AIM method restored kidney cortexes most clearly among the three methods. In Figure 6(C), as in Figure 5(B), the NAC-based method erroneously blurred the spine while CTAC- and AIM did not.

As further demonstrated in Table 2, for the ^{18}F-FPDTBZ studies, all three methods performed equally well for kidney and pancreas ROIs except NAC-based method that blurred the spine. For the ^{18}F-FMISO study, the

differences for the large tumor among three methods were relatively small, since larger tumors are less sensitive to motion. For the small tumor, AIM and NAC-based method slightly outperformed the CTAC-based method. Similar results were found based on signal-to-noise ratios as presented in the Supplemental Table 2.

DISCUSSION

In PET/CT studies, fast helical CT results in mismatched attenuation correction for gated PET, which affects the accuracy of motion estimation and subsequent motion correction. Prior studies considered the NAC-based method (*8*) as an alternative to the CTAC-based approach to avoid CT-mismatch artifact. The NAC-based approach provides satisfactory results for lesions close to the lung-liver interface, but unsatisfactory corrections for lesions in the center of the body. To address such limitations, we presented a fully automated respiratory motion correction framework of AIM, which builds the motion model based on MLACF-reconstructed gated-PET data without mismatched artifact. By comparing to model-building methods using CTAC and NAC-based gated-PET data, AIM showed improvements in terms of SUV_{mean}, SUV_{max}, SUR and SNR for three tracers. The reference phase determination algorithm can successfully identify the PET reference phase that best matches the helical CT attenuation map, regardless of using breath-hold or free-breathing protocols.

In this study, the AIM achieved superior performance by performing event-by-event correction using listmode reconstruction. However, the motion estimation based on attenuation-matched gated-PET data and the reference phase selection method presented in this study can also be applied to sinogram-based motion correction methods, such as PPR and MCIR, which cannot correct for intra-gate motion, but can correct inter-gate motion.

There are several limitations and future directions of the proposed AIM method. First, as shown in the SUR_{AIM} plot (Supplemental Figure 2), ROIs of two patients were under the identity line. These ROIs correspond to lesions at the edge of the spine where spatial motion discontinuities happened. Current FFD registration transformation model with relatively large control point spacing cannot accurately capture this motion, which could explain the bias for the two lesions. Second, parameters used in the study, such as kernel sizes in smoothing filter, were chosen empirically rather than optimal. Future parameter-optimization work is needed. Third, compared to the CTAC-based approach, gated-PET in AIM is noisier due to the transmission-less reconstruction (*17*), which may introduce additional noise-induced errors in motion-estimating registrations, especially for low-dose protocols (*18,19*). To address the potential high noise issue, more sophisticated post-reconstruction denoising algorithms (*20*)

or regularized transmission-less reconstruction algorithms might be needed. Fourth, although AIM is able to identify the reference PET gate that best-matches the CT, there could be changes in the patient's respiratory pattern between CT and PET acquisitions. This will introduce additional CT-mismatch artifacts during the final reconstruction. To address this problem, our INTEX framework would need to warp the CT-μ to match one PET gate based on the estimated motion model (*21*) or directly use the MLAA-μ as the AC-map in the final OSEM reconstruction.

In this study, NMI was used as the similarity metric for motion estimation registration. By trial and error, we found NMI is the most robust metric comparing to other metrics, e.g. sum squared difference and cross correlation. In terms of computation cost, AIM requires N (number of gates) gated reconstructions, N-1 non-rigid registrations and one event-by-event list-mode reconstruction. To make AIM clinically feasible, acceleration with GPU-based list-mode reconstruction might be needed.

CONCLUSION

A new PET/CT respiratory motion correction framework, AIM, has been developed and evaluated. It automatically selects the PET reference phase that best matches the CT, builds a motion model based on attenuation-matched gated-PET data, and corrects inter- and intra-gate respiratory motion in an event-by-event fashion. AIM provided superior motion correction than CTAC- and NAC-based methods, and was shown to be applicable to multiple tracers.

ACKNOWLEGEMENT

This work was funded by a research contract from Siemens Medical Solutions and NIH grant S10RR29245. This work was also supported by NIH grants 1S10RR029245-01 and by CTSA Grant Number UL1 TR000142 from the National Center for Advancing Translational Science (NIH). Its contents are solely the responsibility of the authors and do not necessarily represent the official view of NIH.

REFERENCES

1. Xu Q, Yuan K, Ye D. Respiratory motion blur identification and reduction in ungated thoracic PET imaging. *Phys Med Biol.* 2011;56:4481-4498.

2. Goerres GW, Burger C, Kamel E, et al. Respiration-induced attenuation artifact at PET/CT: Technical considerations. *Radiology.* 2003;226:906-910.

3. Osman MM, Cohade C, Nakamoto Y, Marshall LT, Leal JP, Wahl RL. Clinically significant inaccurate localization of lesions with PET/CT: frequency in 300 patients. *J Nucl Med.* 2003;44:240-243.

4. Liu C, Pierce LA, Alessio AM, Kinahan PE. The impact of respiratory motion on tumor quantification and delineation in static PET/CT imaging. *Physics in Medicine and Biology.* 2009;54:7345-7362.

5. Nehmeh SA, Erdi YE, Ling CC, et al. Effect of respiratory gating on quantifying PET images of lung cancer. *Journal of Nuclear Medicine.* 2002;43:876-881.

6. Klein GJ, Reutter BW, Huesman RH. Four-dimensional affine registration models for respiratory-gated PET. *Ieee Transactions on Nuclear Science.* 2001;48:756-760.

7. Lamare F, Carbayo MJL, Cresson T, et al. List-mode-based reconstruction for respiratory motion correction in PET using non-rigid body transformations. *Physics in Medicine and Biology.* 2007;52:5187-5204.

8. Fayad HJ, Lamare F, Le Rest CC, Bettinardi V, Visvikis D. Generation of 4-dimensional CT images based on 4-dimensional PET-derived motion fields. *J Nucl Med.* 2013;54:631-638.

9. Panin VY, Defrise M, Nuyts J, Rezaei A, Casey ME. Reconstruction of uniform sensitivity emission image with partially known axial attenuation information in PET-CT scanners. Paper presented at: IEEE NSS/MIC, 2012; Anaheim CA, USA.

10. Panin VY, Aykac M, Casey ME. Simultaneous reconstruction of emission activity and attenuation coefficient distribution from TOF data, acquired with external transmission source. *Physics in Medicine and Biology.* 2013;58:3649-3669.

11. Chan C, Onofrey J, Jian Y, et al. Non-rigid Event-by-event Continuous Respiratory Motion Compensated Listmode Reconstruction for PET. *IEEE Trans of Medical Imaging.* 2017.

12. Jin X, Chan C, Mulnix T, et al. List-mode reconstruction for the Biograph mCT with physics modeling and event-by-event motion correction. *Physics in Medicine and Biology.* 2013;58:5567-5591.

13. Normandin MD, Petersen KF, Ding YS, et al. In vivo imaging of endogenous pancreatic beta-cell mass in healthy and type 1 diabetic subjects using 18F-fluoropropyl-dihydrotetrabenazine and PET. *J Nucl Med.* 2012;53:908-916.

14. Carlin S, Humm JL. PET of hypoxia: current and future perspectives. *J Nucl Med.* 2012;53:1171-1174.

15. Joshi A, Scheinost D, Okuda H, et al. Unified framework for development, deployment and robust testing of neuroimaging algorithms. *Neuroinformatics.* 2011;9:69-84.

16. Rueckert D, Sonoda LI, Hayes C, Hill DLG, Leach MO, Hawkes DJ. Nonrigid registration using free-form deformations: Application to breast MR images. *Ieee Transactions on Medical Imaging.* 1999;18:712-721.

17. Rezaei A, Defrise M, Bal G, et al. Simultaneous reconstruction of activity and attenuation in time-of-flight PET. *IEEE Trans Med Imaging.* 2012;31:2224-2233.

18. Lu Y, Fontaine K, Germino M, et al. Investigation of sub-centimeter lung nodule quantification for low-dose PET. *IEEE Transactions on Radiation and Plasma Medical Sciences.* 2018;2:1-10.

19. Schaefferkoetter JD, Yan J, Sjöholm T, et al. Quantitative accuracy and lesion detectability of low-dose 18F-FDG PET for lung cancer screening. *Journal of Nuclear Medicine.* 2017;58:399-405.

20. Chen Y, Shi L, Feng Q, et al. Artifact suppressed dictionary learning for low-dose CT image processing. *IEEE Trans Med Imaging.* 2014;33:2271-2292.

21. Rezaei A, Michel C, Casey ME, Nuyts J. Simultaneous reconstruction of the activity image and registration of the CT image in TOF-PET. *Physics in Medicine and Biology.* 2016;61:1852-1874.

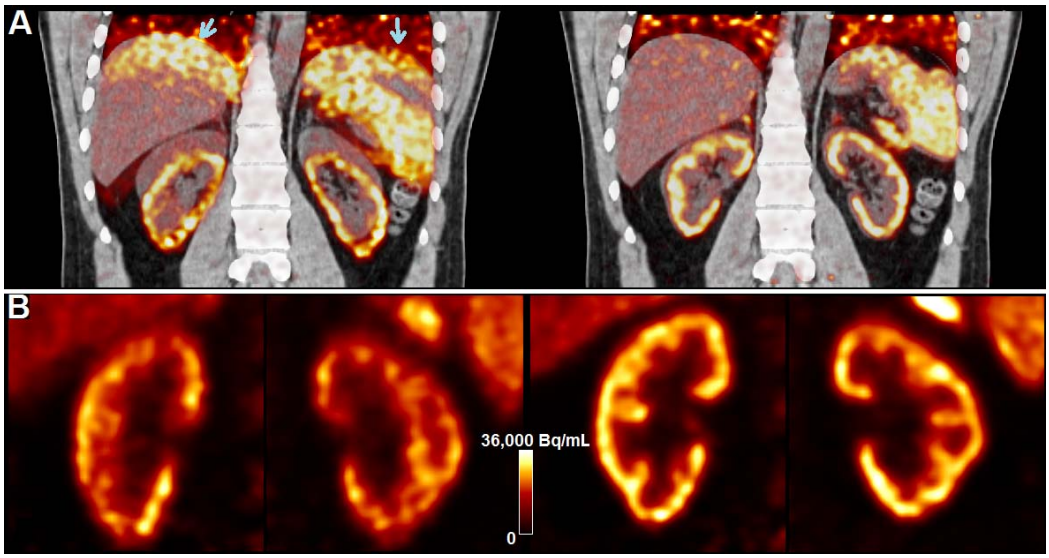

Figure 1. A. Inspiration- (left) and expiration- (right) phase gated PET reconstructions superposed with CT for a sample ^{18}F-FPDTBZ study. Arrows in A (left) point to attenuation-mismatch. B. Inspiration- (left) and expiration- (right) phase PET reconstruction of kidneys.

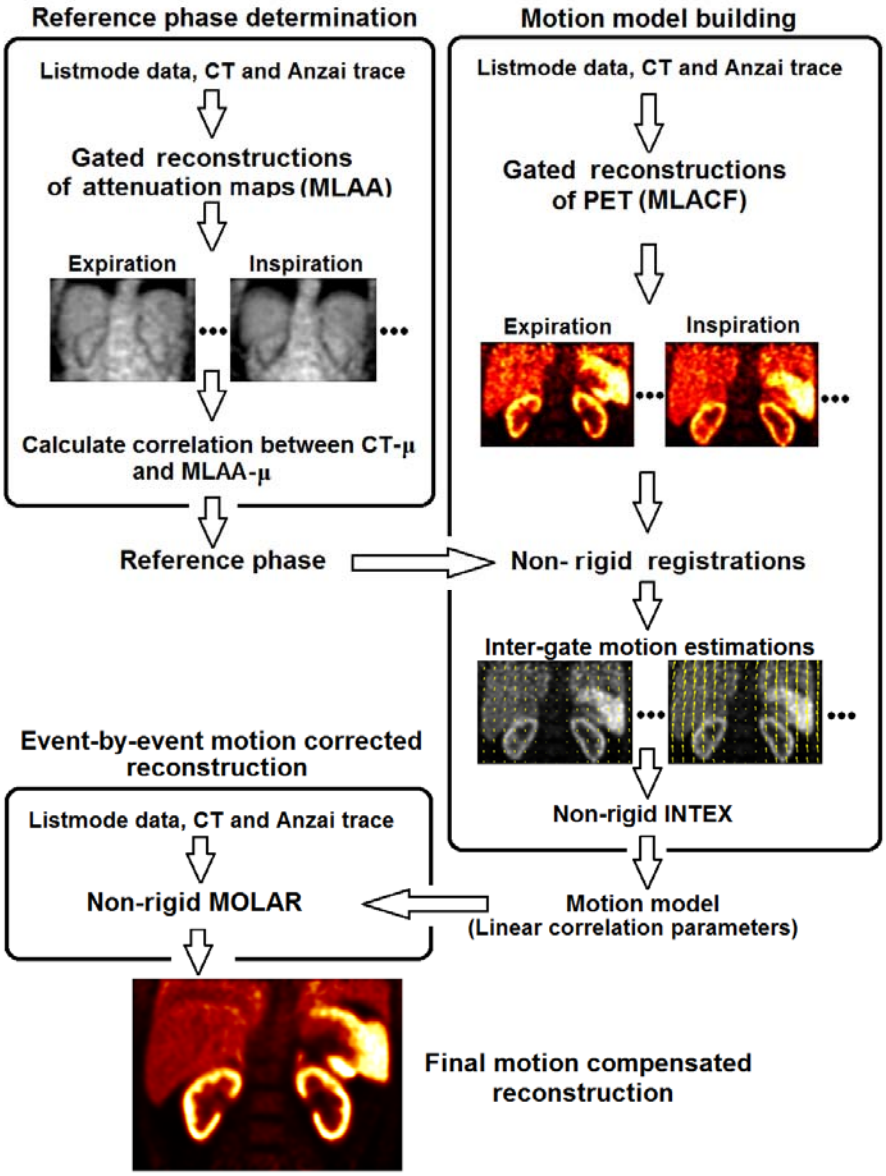

Figure 2. Flowchart of AIM framework, consisting of 1) reference phase determination, 2) motion model building, and 3) event-by-event motion correction.

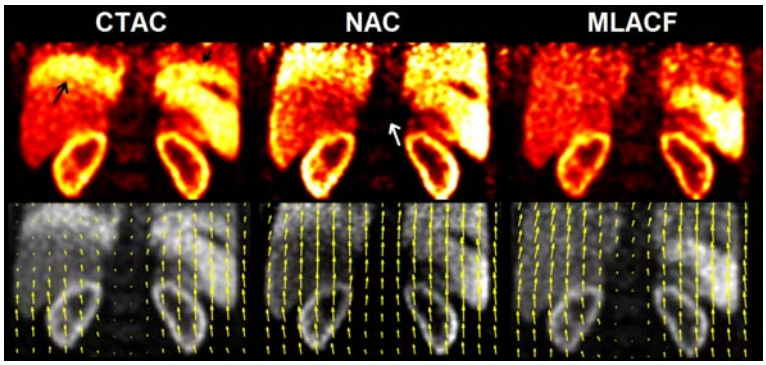

Figure 3. End-inspiration gated reconstructions using different attenuation correction methods (top row) and EI-EE motion vectors derived from each method, superposed on the EI reconstructions (bottom) for ^{18}F-FPDTBZ study #1.

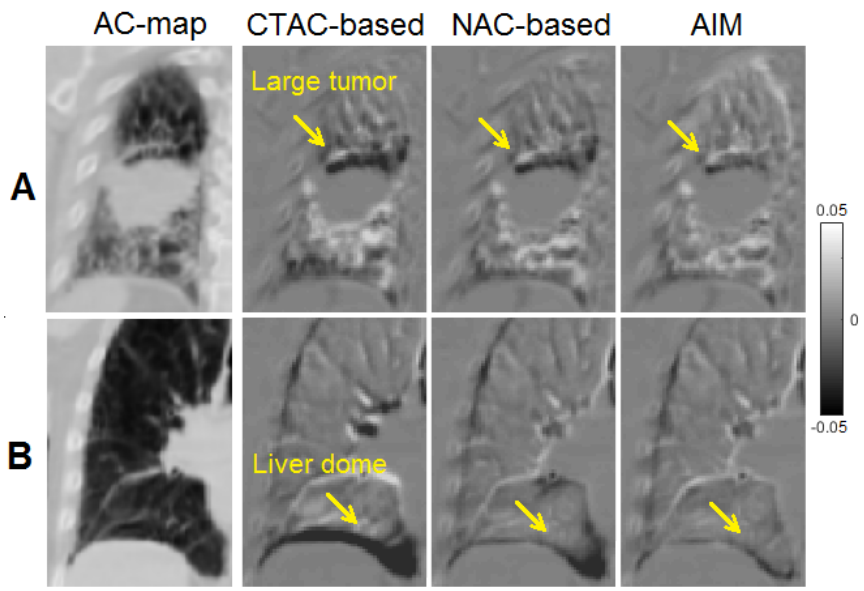

Figure 4. Difference images between μ_{4DCT} and μ_{Syn} at EI gate. The right three columns represent the results of the CTAC-based, NAC-based, and AIM methods, respectively. AC-map is shown as the reference. (A) Coronal slice at right-lung region with a large tumor. The yellow arrow points to the top of the tumor. (B) Coronal slice of the right-lung region, where the yellow arrows point to the liver-lung border.

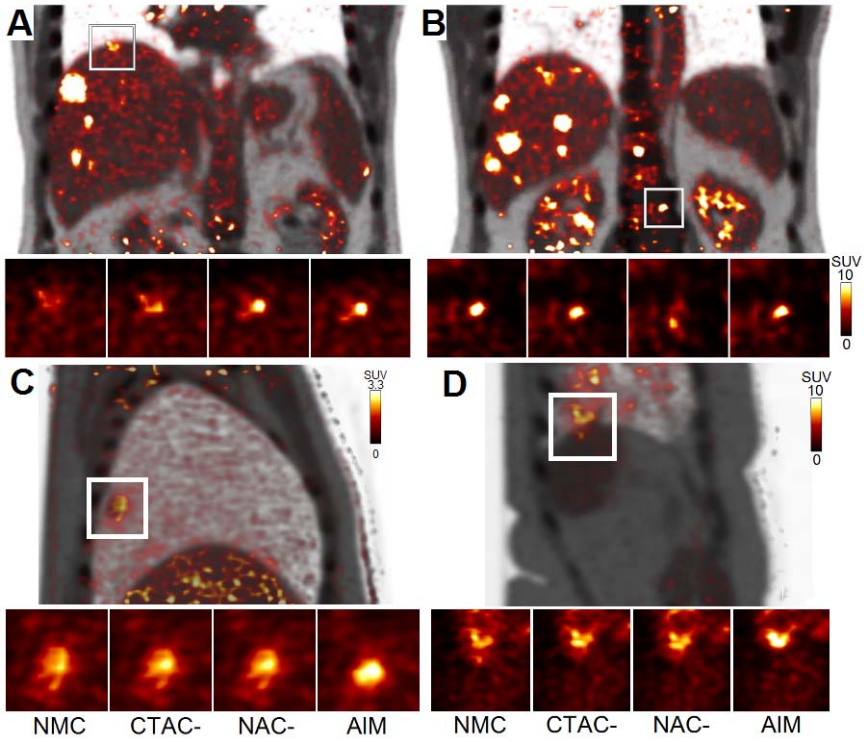

Figure 5. Sample slices of final motion-corrected reconstructions of ^{18}F-FDG studies. A and B show coronal slices from Study #2. C shows Study #3, and D shows Study #9. PET and CT fused images are shown for the whole FOV. Zoomed-in images of local ROIs show results for no motion correction (NMC) and different correction methods.

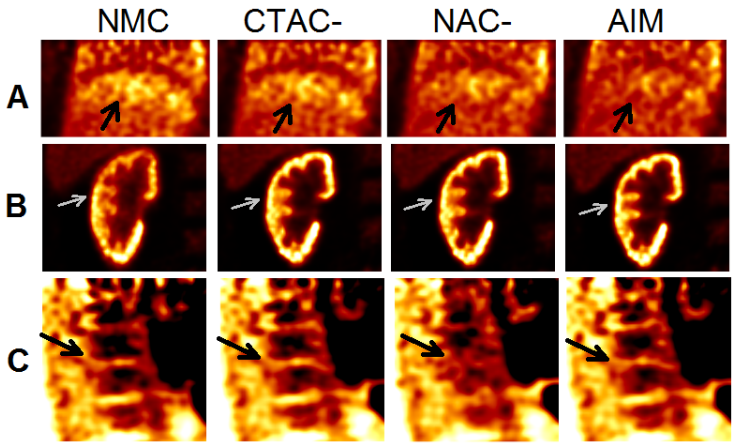

Figure 6. Final reconstruction examples of ^{18}F-FPDTBZ studies with different correction methods. (A) Coronal-liver-lung region for study #1. Black arrows point to the lung-liver border. (B) coronal-right-kidney region for study #2. Arrows points to the right-kidney cortex. (C) Sagittal spine region for study #1. Arrows points to bone marrow gap.

Table 1. Percent error ($\mu Err\%(g)$) ± standard deviation for various ROIs for the ^{18}F-FMISO validation study comparing PET-based and 4D-CT-based motion estimation. Standard deviation is calculated across all gates.

ROI Region	CTAC-based	NAC-based	AIM
Liver-dome	13.9±19.9%	4.9±8.7%	3.2±4.4%
Large tumor (mid-right)	2.2±7.0%	1.8±6.3%	-1.3±2.0%
Small tumor (mid-left)	-7.1±2.6%	-6.3±2.5%	-4.3±2.2%

Table 2 Percent increases in SUV_{mean}, SUV_{max} and SUR.

Tracer	Study	# of ROIs	Motion Amp. (mm) ǂ	SUV_{mean}+%			SUV_{max}+%			SUR +%		
				CTAC-	NAC-	AIM	CTAC-	NAC-	AIM	CTAC-	NAC-	AIM
^{18}F-FDG	1	17	5.3(2.0-8.3)	16.7±19.5	18.2±19.2	21.1±18.4	13.9±14.4	15.6±16.0	15.6±10.0	33.2±22.3	35.0±21.9	40.5±21.3
	2	106	5.4(1.7-9.4)	24.6±26.6	22.4±23.5	28.0±28.7	19.7±22.5	21.2±26.1	22.6±24.2	26.5±27.0	21.1±23.3	27.9±26.8
	3	1	6.9	6.9	4.9	20.2	-0.4	0.1	20.5	13.2	7.8	26.9
	4	25	8.4(2.5-16.2)	38.5±48.8	30.8±48.8	42.2±50.3	26.6±50.0	20.9±50.6	29.2±57.0	37.3±48.4	29.5±48.3	43.1±50.6
	5	28	8.3(3.8-25.2)	13±19.4	16.3±21.2	19.3±20.6	10.6±23.8	14.5±28.9	11.2±21.1	12.0±19.2	15.2±21.0	19.3±20.6
	6	3	3.0(1.6-4.2)	7.0±3.8	2.8±6.8	10.2±2.0	6.4±5.7	2.0±5.9	6.6±4.5	6.7±3.8	0.4±6.6	9.8±2.0
	7	3	3.6(1.3-5.8)	2.6±2.7	3.5±3.3	5.6±3.5	5.2±6.1	2.6±6.2	5.9±5.6	9.6±2.9	11.7±3.6	11.9±3.8
	8	88	8.7(1.8-14.0)	24.9±20.1	25.3±19.9	31.3±23.2	23.1±19.5	23.8±19.3	27.7±20.6	19.6±19.3	21.3±19.3	28.0±22.7
	9	36	7.0(1.8-14.7)	2.9±7.5	5.7±6.5	15.1±12.7	-0.1±13.6	2.8±12.3	9.3±14.5	-1.5±7.2	2.4±6.3	12.2±12.4
	10	16	4.6(2.6-7.3)	3.4±7.1	2.0±10.0	5.7±7.9	3.2±6.1	2.4±12.6	5.9±11.0	19.9±8.3	17.4±11.5	21.7±9.1
	Study Level mean	**10 studies (323 ROIs)**	**6.1**	**14.0**	**13.2**	**19.9**	**10.8**	**10.6**	**15.5**	**17.6**	**16.2**	**24.1**
^{18}F-FPDTBZ	1	Kidney	11.7	24.3	28.8	28.5	6.9	8.3	9.9	26.6	28.6	32.0
		Pancreas	9.2	23.1	28.3	27.9	5.8	8.6	8.2	25.4	28.0	31.4
		Spine	1.4	-3.1	-19.7	-2.9	-2.0	-21.6	-1.9	-1.3	-19.9	-0.3
	2*	Kidney	14.7	31.2	25.7	34.4	20.3	23.0	21.9	-	-	-
		Pancreas	14.2	17.5	17.7	17.9	5.4	5.0	5.3	-	-	-
		Spine	2.8	-0.7	-35.6	-1.6	-3.8	-24.0	-5.5	-	-	-
^{18}F-FMISO	1	Large tumor (avid area)	11.8	9.6	10.9	11.1	1.6	1.9	2.1	12.9	14.9	14.9
		Small tumor	5.3	15.0	21.1	21.6	8.6	17.1	17.3	18.4	25.5	25.8

* No SUR result is reported for study 2 since the heart was out of FOV

ǂ Mean and range of motion amplitudes estimated between end-inspiration and end-expiration gates across all lesions for each subject.

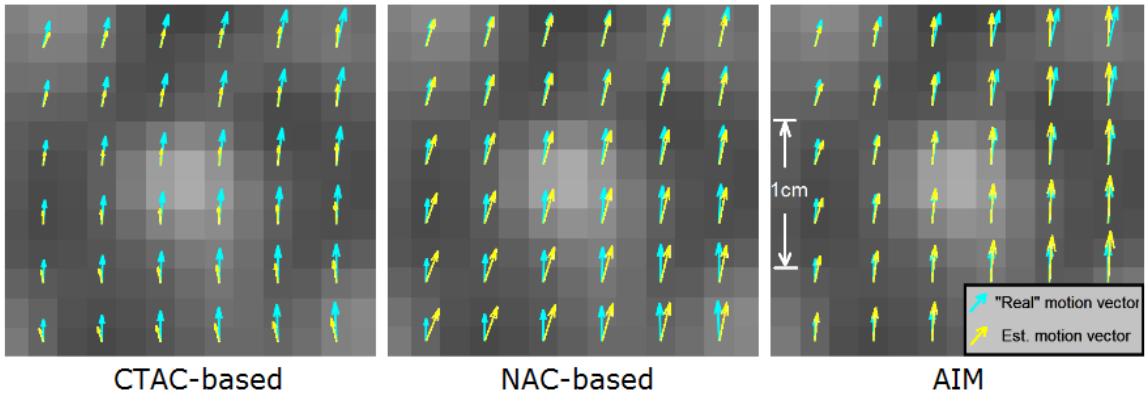

SUPPLEMENTAL FIGURE 1. Comparison of estimated motion vectors generated by different approaches at small tumor region of the ^{18}F-FMISO study. Background for each subfigure is the gated-PET AIM at end-expiration (EE). Blue arrows represent motion vectors ("real") generated by registration between EE and end-inspiration (EI) 4D-CT, and are repeated for each sub figure. Yellow arrows represent motion vectors generated by registration between EE and EI gated-PET using different approaches. All vectors point from EI to EE phase. AIM shows the best alignment between estimated motion vector and real motion vector.

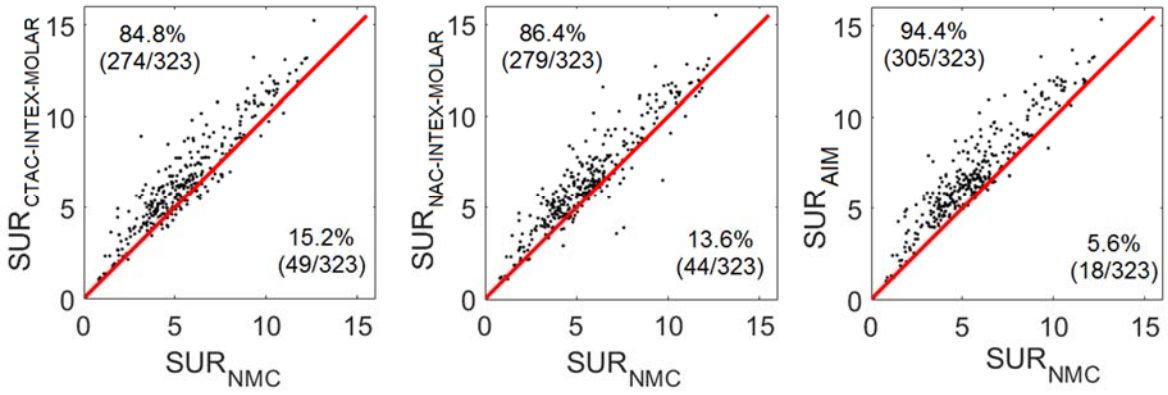

SUPPLEMENTAL FIGURE 2. SUR-improvement results of all ROIs from all ^{18}F-FDG studies for three correction methods. Each dot represents one ROI. Dots above the red line of identity indicates a SUR increase after motion correction while below indicates a decrease. Percentage Values number shows percentage/numbers of ROIs falls above or below the red identity line.

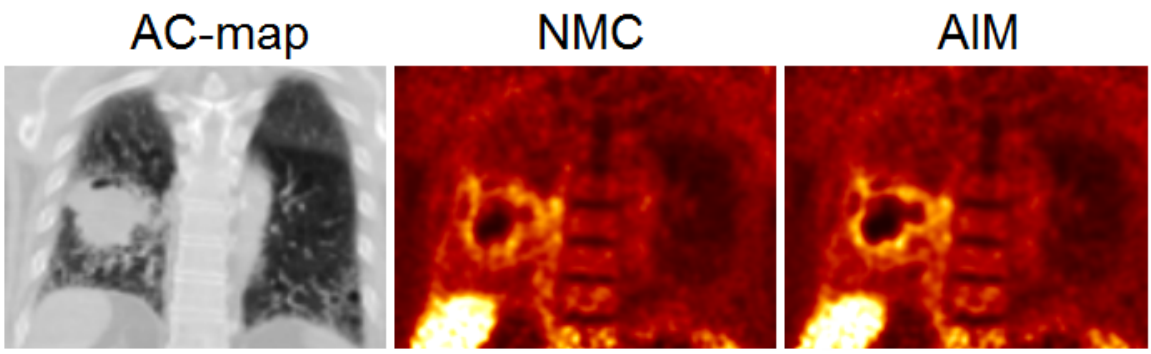

SUPPLEMENTAL FIGURE 3. Reconstruction results of the ^{18}F-FMISO study. A coronal slice through the center of the large hypoxia tumor is shown. Attenuation map (AC-map) is shown as the reference. AIM shows great improvements over NMC (no motion correction) in terms of tumor contrast, delineation of the avid hypoxic area. AIM results could more accurately guide radiation therapy planning, in particular dose painting.

SUPPLEMENTAL TABLE 1. Reference phase determination results

Tracer	Study	Determined reference phase using the proposed method (Predefined phase based on acquisition protocol)
^{18}F-FDG	1	1(F)
	2	1(F)
	3	1(F)
	4	1(F)
	5	1(F)
	6	2(F)
	7	1(F)
	8	1(F)
	9	3(F)
	10	1(F)
^{18}F-FP(+)DTBZ	1	5(5)
	2	1(5)
^{18}F-FMISO	1	3(5)

Note, phase 1 presents end-inspiration (EI) and phase 5 represents end-expiration (EE), phases 2-4 are between EI and EE. F presents free-breathing.

SUPPLEMENTAL TABLE 2.

Coefficient of Variation (CoV) and percent increases in signal-to-noise ratio (SNR).

Tracer	Study *	Body Parts Covered by PET FOV	CoV of background					SNR_{mean}+%		
			NMC	CTAC-	NAC-	AIM	# of ROIs	CTAC-	NAC-	AIM
^{18}F-FDG	1	Abdominal	0.24	0.23	0.22	0.23	17	23.9±20.7	27.7±20.8	29.3±19.6
	2	Abdominal	0.24	0.24	0.23	0.24	106	25.9±26.8	25.8±24.2	27.2±28.5
	3	Thorax	0.30	0.30	0.30	0.33	1	9.2	7.2	12.9
	4	Abdominal	0.24	0.22	0.23	0.22	25	55.5±54.8	42.7±53.2	59.1±56.3
	5	Thorax	0.42	0.40	0.40	0.42	28	23.5±21.2	25.4±22.8	28.6±22.2
	6	Thorax	0.23	0.22	0.21	0.22	3	14.1±3.7	10.9±6.4	16.8±4.1
	7	Thorax	0.22	0.19	0.19	0.20	3	16.3±10.9	16.7±10.4	15.2±9.2
	8	Thorax	0.42	0.43	0.43	0.43	88	29.3±19.2	28.1±18.7	31.0±21.0
	9	Abdominal	0.26	0.25	0.25	0.25	36	1.5±7.4	2.6±6.3	12.6±12.5
	10	Thorax	0.32	0.30	0.31	0.31	16	14.5±13.1	9.2±14.1	13.6±12.7
							Study Level mean 10 studies (323 ROIs)	**21.4**	**19.6**	**24.6**
^{18}F-FPDTBZ	1	Abdominal	0.11	0.10	0.10	0.10	Kidney	29.9	34.9	34.2
							Pancreas	28.7	34.2	33.7
							Spine	1.3	-16	1.4
	2	Abdominal	0.12	0.12	0.12	0.12	Kidney	31.2	25.7	34.4
							Pancreas	17.5	17.7	17.9
							Spine	-0.7	-35.6	-1.6
^{18}F-FMISO	1	Thorax	0.15	0.15	0.15	0.15	Large tumor (avid area)	10.1	11.6	11.5
							Small tumor	15.5	21.9	22.1

For abdominal FOV, noise is defined as the standard deviation inside a ROI placed on the liver. CoV is defined as the standard deviation divided by the mean within the liver ROI; For thorax FOV, noise is defined as the standard deviation inside a ROI placed in the lung. CoV is defined as the standard deviation divided by the mean within the lung ROI.